Journal of Alloys and Compounds 501 (2010) 227–232

Contents lists available at ScienceDirect

Journal of Alloys and Compounds

journal homepage: www.elsevier.com/locate/jallcom

Effect of Zr on the thermal stability and magnetic properties of $Fe_{78}Si_9B_{13}$ glassy alloy

H.J. Ma[a], J.T. Zhang[a], G.H. Li[a], W.X. Zhang[b], W.M. Wang[a,*]

[a] Key Laboratory for Liquid-Solid Structural Evolution and Processing of Materials (Ministry of Education), Shandong University, Jinan 250061, China
[b] State Key Laboratory of Electronic Thin Films and Integrated Devices, University of Electronic Science and Technology of China, Chengdu 610054, China

ARTICLE INFO

Article history:
Received 1 March 2010
Received in revised form 28 March 2010
Accepted 1 April 2010
Available online 20 April 2010

Keywords:
Thermal stability
Thermal expansion
Magnetic properties

ABSTRACT

The $(Fe_{0.78}Si_{0.09}B_{0.13})_{100-x}Zr_x$ ($x=0$, 1 and 2) glassy alloys have been investigated in this paper. The experimental results show that the minor addition of Zr can improve the thermal stability of the Fe-based alloy. The thermal contraction process of the ribbons is mainly dependent on the crystallization process. With increasing Zr content (c_{Zr}), the difference (Δd) between the nearest neighbor distance (d_{exp}) deduced from the X-ray diffraction pattern and the estimated nearest neighbor distance d_{cal}, the onset crystalline temperature (T_x), the reduced crystalline temperature (T_{rx}), the apparent activation energy (E_{p1}) for the first crystallization, and the difference ($\Delta\alpha$) between the expansion coefficients of amorphous ribbons (α_{amor}) and fully crystallized counterparts (α_{cryst}) of the Fe-based glassy alloys first increase and then decrease, which is opposite to the change of the saturation magnetization (M_s). The variation of these parameters can be explained by the deviation degree from the equilibrium state of the amorphous ribbons. Besides the M–T measurement, the Curie temperature (T_c) of the Fe-based glassy alloys can also be scaled by the bump and inflection temperatures ($T_{c,dsc}$ and T_k) in differential scanning calorimetric and dilatometric curves, respectively, showing a slight decreasing tendency with increasing c_{Zr}.

1. Introduction

Among all the glassy alloys, Fe-based glassy alloys were firstly commercialized in the industry. Up to now, the Fe-based glassy alloys have still attracted great interest because of its low cost, good corrosion resistance, and good mechanical and soft-magnetic properties. The newly developed Fe-based glassy alloys can be classified into two groups. One group is the paramagnetic Fe-based glassy alloys named amorphous steels and developed by Ponnambalam et al. [1] and Lu et al. [2]. The other group is soft/hard-magnetic Fe-based glassy alloys and obtained by adding of transition metals, metalloids and rare earth elements into the conventional Fe-metalloids (B, C, Si and P) amorphous alloys [3,4]. Both groups of Fe-based glassy alloys show an attractive utilization prospect in functional and structural material domains.

Thermal expansion behavior is one of the most important thermodynamic characteristics and is strongly correlated with the amorphous structure of metallic glasses [5–7]. When the metallic melts are quenched into amorphous state, some free volume is frozen in the as-quenched amorphous alloy [8,9]. In the heating process of the thermal dilatometric (DIL) measurement, the annihilation of free volume, the structural relaxation and the crystallization of metallic glasses affect the thermal expansion coefficient [10]. Accordingly, the studies on the thermal expansion behavior can deepen our understanding of the microstructure evolution of the Fe-based glassy alloys.

Recently, by adding minor metallic element to the conventional Fe-Si-B based glassy alloy, Makinoa et al. found that the minor metal elements can enhance the glass forming ability (GFA) but deteriorate the magnetic properties of the Fe-based glassy alloys [3]. Our preliminary work has showed that small amount of nickel addition can deteriorate the magnetic property of Fe–Si–B-based glassy alloys as well [11]. Therefore, it is useful to obtain further information about the effect of minor addition on the behavior and microstructure evolution of the Fe-based glassy alloys. As a well known glass-forming element, small amount of zirconium addition could enhance the GFA and improve the soft magnetic properties in Co- and Fe-based glassy alloys [12,13]. Especially in the Fe–B-based glassy alloys, Zr can form a reinforced 'backbone' with boron which enhances the stability of the undercooled melt and suppress the crystallization [14].

In present work, we choose the $Fe_{78}Si_9B_{13}$ alloy as the starting alloy and add small amount of Zr to it. The alloys with nominal composition of $(Fe_{0.78}Si_{0.09}B_{0.13})_{100-x}Zr_x$ ($x=0$, 1 and 2) have been successfully fabricated by melt-spinning. The major objective of this work is to investigate the effect of Zr on the thermal stability,

---

* Corresponding author. Tel.: +86 0531 88392749; fax: +86 0531 88395011.
E-mail address: weiminw@sdu.edu.cn (W.M. Wang).

0925-8388/$ – see front matter © 2010 Elsevier B.V. All rights reserved.
doi:10.1016/j.jallcom.2010.04.075

thermal expansion behavior, and magnetic properties of Fe–Si–B-based glassy alloy and try to provide new knowledge on the effect of transition metal elements in designing Fe-based amorphous alloys.

2. Experimental procedures

The master alloy ingot with a nominal composition of $Fe_{78}Si_9B_{13}$ was supplied by the National Amorphous Nanocrystalline Alloy Engineering Research Center of China. The ingot and zirconium (99.9 mass%) were put into a quartz tube and were spun using a single copper roller in the air. The diameter of the copper roller was 35 cm, and the circumferential speed was 36.6 m/s. The obtained ribbons with nominal composition of $(Fe_{0.78}Si_{0.09}B_{0.13})_{100-x}Zr_x$ ($x = 0$, 1 and 2, labeled as C0, C1 and C2) were 20–50 μm in thickness and 2–5 mm in width.

The samples were investigated by X-ray diffraction (XRD, Cu Kα, $\lambda = 0.15405$ nm). In the XRD measurements, the step size was 0.02° with a count time of 4°/min. The central positions $2\theta_{max}$ of the diffusive amorphous maximum were used to give the nearest neighbor distance in the structural units of the glasses by following equation [15]:

$$d = \frac{7.7}{k}, \quad \text{with } k = \frac{4\pi \sin\theta}{\lambda} \tag{1}$$

here λ, the wavelength of the X-ray used, was 0.15405 nm.

The amorphous ribbons were analyzed by a differential scanning calorimeter (DSC, Netzsch DSC404) with different heating rates (10, 20, 30 and 40 K/min), respectively. By using Kissinger method, the apparent activation energies of the present alloys were calculated by means of the following equation [16]:

$$\ln\left(\frac{\Phi}{T_p^2}\right) = -\frac{E}{T_p} + \text{const} \tag{2}$$

where E is the apparent active energy, R the gas constant, Φ the scanning heating rate and T_p the characteristic temperature of the crystallization.

The dilatometric measurements were performed using a dilatometer (DIL, Netzsch DIL402C) in argon atmosphere at a heating rate of 10 K/min. The dilatometric samples were made by overlapping the as-spun $(Fe_{0.78}Si_{0.09}B_{0.13})_{100-x}Zr_x$ amorphous ribbons into blocks with copper wires. The length, width and height of the samples were about 13, 3 and 3 mm, respectively. And the applied load during the measurement was 25 cN.

The magnetic properties were measured by vibrating sample magnetometer (VSM).The M–H hysteresis loops were measured under a maximum field of 6000 Oe. The temperature–magnetization curves (M–T) were measured under a temperature range of 298–1073 K with a heating rate of 5 K/min. The Curie temperatures (T_c) were calculated using the equation [17]:

$$M(T) = M(0)\left(1 - \frac{T}{T_c}\right)^{\beta} \tag{3}$$

where $M(0)$ is the saturation magnetization at 0 K, β a constant equal to 0.36. When we plot the curve of $M^{1/\beta}$–T, its interception point with line $M = 0$ is the Curie temperature T_c.

3. Results

Fig. 1 shows the X-ray diffraction spectra of the as-spun $(Fe_{0.78}Si_{0.09}B_{0.13})_{100-x}Zr_x$ ($x = 0$, 1 and 2, labeled as C0, C1 and C2) ribbons. All the ribbons exhibit a typical diffusive diffraction maximum characteristic for an amorphous phase without any crystalline peak. The inset gives the Gaussian fitting peaks in the vicinity of the diffusive maxima. Obviously, their location ($2\theta_{max}$) tends to shift toward the lower values with increasing Zr content (c_{Zr}). Based on the measured $2\theta_{max}$, the nearest neighbor distances (d_{exp}) of the as-spun ribbons have been calculated according to Eq. (1). The estimated nearest neighbor distance d_{cal} of one alloy can be calculated using the following expression:

$$d_{cal} = \sum c_i d_i \tag{4}$$

where d_i denotes the covalent radius of the ith constituent element in the crystalline state, cited from [18], and c_i is the atomic percent of the ith constituent element. The experimental d_{exp}, the calculated d_{cal} and their difference (Δd) are listed in Table 1. Here the d_{exp} and d_{cal} of the ribbons increase with increasing c_{Zr}, due to the addition of the large Zr atoms. However, Δd varies in the following order: C0 < C2 < C1.

Fig. 2 shows the DSC curves of the crystallization process, the melting and solidification processes for the as-spun

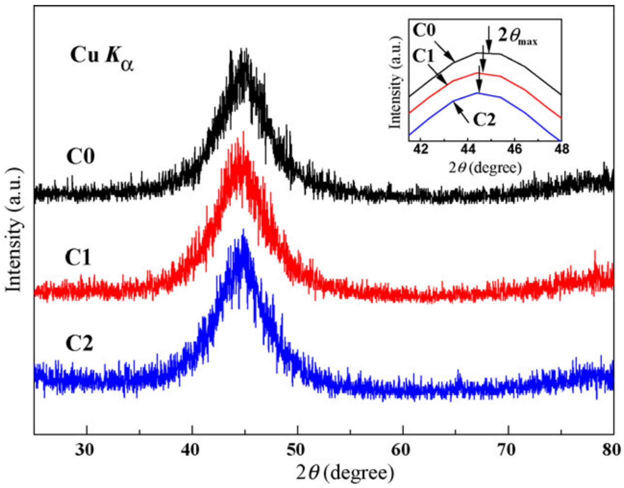

Fig. 1. XRD patterns of the as-spun $(Fe_{0.78}Si_{0.09}B_{0.13})_{100-x}Zr_x$ ($x = 0$, 1 and 2) glassy alloys. The inset gives the large magnification of Gaussian fitting curves for the diffusive maxima.

Table 1
Nearest neighbor distance (d_{exp}), the calculated nearest neighbor distance (d_{cal}) by the covalent radius and their difference Δd of as-spun Fe-based ribbons.

Alloys	d_{exp} (nm)	d_{cal} (nm)	Δd (nm)
$Fe_{78}Si_9B_{13}$(C0)	0.2477 ± 0.0001	0.2363	0.0114 ± 0.0001
$(Fe_{0.78}Si_{0.9}B_{0.13})_{99}Zr_1$(C1)	0.2487 ± 0.0001	0.2369	0.0118 ± 0.0001
$(Fe_{0.78}Si_{0.9}B_{0.13})_{98}Zr_2$(C2)	0.2490 ± 0.0001	0.2375	0.0115 ± 0.0001

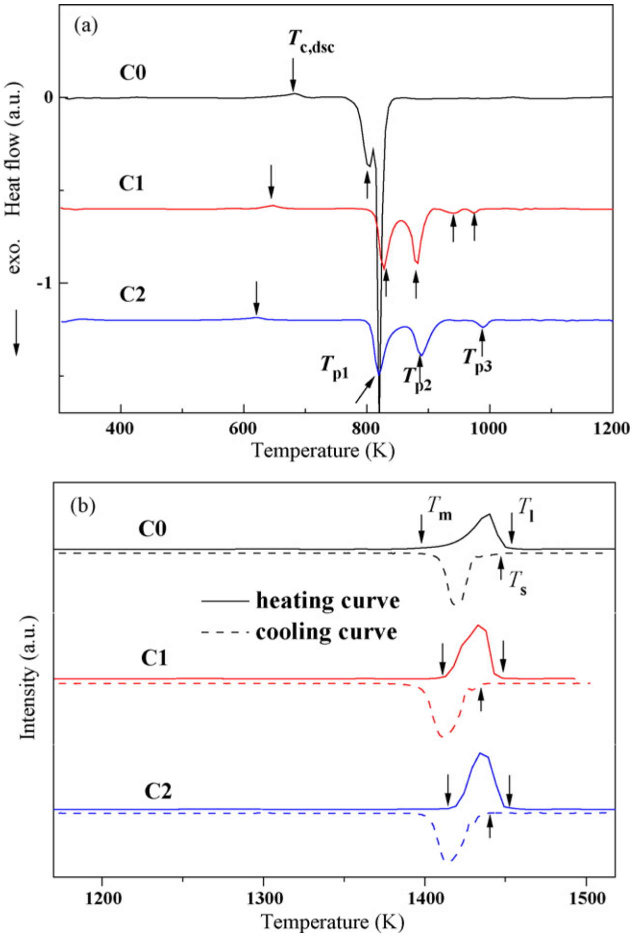

Fig. 2. DSC curves of the $(Fe_{0.78}Si_{0.09}B_{0.13})_{100-x}Zr_x$ ($x = 0$, 1 and 2) glassy alloys with a heating rate of 10 K/min for (a) crystallization process and (b) melting and solidification processes.

Table 2
Curie temperatures ($T_{c,dsc}$) deduced from DSC scans of the Fe-based amorphous ribbons at different heating rates.

Alloys	10 K/min	20 K/min	30 K/min	40 K/min
$Fe_{78}Si_9B_{13}$(C0)	685	684	681	680
$(Fe_{0.78}Si_{0.9}B_{0.13})_{99}Zr_1$(C1)	647	645	645	646
$(Fe_{0.78}Si_{0.9}B_{0.13})_{98}Zr_2$(C2)	620	621	621	620

$(Fe_{0.78}Si_{0.09}B_{0.13})_{100-x}Zr_x$ ($x = 0$, 1 and 2) ribbons with a heating rate of 10 K/min. There are two, four and three exothermic peaks in DSC curves of C0, C1 and C2 ribbons, respectively (Fig. 2a). Here, the exothermic peaks are denoted by T_{p1}, T_{p2}, T_{p3} and T_{p4}, it is found that the temperature interval between T_{p1} and T_{p2} increases with c_{Zr}, suggesting that Zr can restricts the eutectic crystallization of the amorphous ribbon, which is similar to the effect of Cu and Ni in $Fe_{73.5}Nb_3Cu_1Si_{13.5}B_9$ glassy alloy [19]. In addition, a slight endothermic bump before the first exothermic peak can be seen in the DSC curves, which is also visible in the DSC curves with heating rates of 20, 30 and 40 K/min (not shown in this paper). This bump resulted from the Curie transition [20] is denoted by $T_{c,dsc}$ in Fig. 2a. The $T_{c,dsc}$ values at different heating rates are listed in Table 2. It is shown that the $T_{c,dsc}$ of the C0 alloy decreases with increasing heating rate, but the $T_{c,dsc}$ of the C1 and C2 alloys changes little with the variation of heating rate. Moreover, the onset crystalline temperature (T_x), which characterize the thermal stability of amorphous alloys, first increase and then decrease with increasing c_{Zr}, indicating that the thermal stability of the present alloys is in this order: C0 < C2 < C1, which is consistent with the Δd of these ribbons.

During the melting process, as shown in Fig. 2b, there is only one endothermic peak for the three samples. However, the cooling curves exhibit two exothermic peaks and the first small peak start from the onset temperature of solidification (T_s) in the cooling curves may be due to the formation of bcc-Fe or FeB compounds. The onset temperature of crystallization T_x, the first, second, third and fourth crystallization peak temperatures T_{p1}, T_{p2}, T_{p3} and T_{p4}, the onset and end temperatures of the melting process T_m and T_l, the temperature interval (ΔT_m) between T_m and T_l, and the reduced crystalline temperature (T_{rx}) at a heating rate of 10 K/min are listed in Table 3. It is known that ΔT_m and T_{rx} can characterize the thermal stability of the glassy alloys, the narrower the ΔT_m and the larger the T_{rx}, the better the thermal stability [21,22]. Hence, according to ΔT_m and T_{rx} in Table 3, it can be seen that minor addition of Zr can improve the thermal stability of $Fe_{78}Si_9B_{13}$ alloy and that the C1 alloy exhibits a better thermal stability than the C0 and C2 alloys. Here the order of thermal stability of the ribbons is C0 < C2 < C1, agreeing with Δd and T_x.

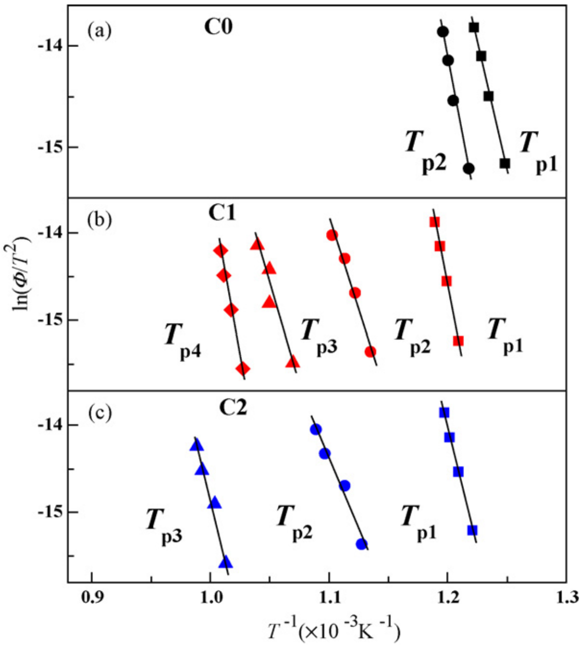

Fig. 3. Kissinger plots of $\ln(\Phi/T^2)$ against $1/T$ for T_{p1}, T_{p2}, T_{p3} and T_{p4} of $(Fe_{0.78}Si_{0.09}B_{0.13})_{100-x}Zr_x$ ($x = 0$, 1 and 2) glassy alloys. (a) C0, (b) C1 and (c) C2.

The DSC curves with heating rates of 20, 30 and 40 K/min (not given in this paper) show that T_x, T_{p1}, T_{p2}, T_{p3} and T_{p4} shift towards higher temperature with increasing heating rate (Φ). According to Eq. (2), the Kissinger plots, i.e. $\ln(\Phi/T_p^2)$ vs $1/T_p$, are depicted in Fig. 3. Apparently, the $\ln(\Phi/T_p^2)$ for the crystallization of each ribbon is linear with $1/T_p$, which can be fitted by a line. Accordingly, the apparent activation energies of the ribbons are obtained and listed in Table 4. The apparent activation energy of the first crystallization peak (E_{p1}) of the C1 alloy is larger than that of the C0 and C2 alloys, and the E_{p1} of the ribbons follows the order of C0 < C2 < C1, agreeing with the variation of the glass thermal stability parameter T_x (Table 3). However, the E_{p2} of the second crystallization peak decreases with c_{Zr}, which is opposite to the variation of onset temperature of the second crystallization (Fig. 2a). Generally, the onset temperature is strongly associated with the nucleation barrier in crystallization [23], and it is considered that the apparent activation energy E calculated by Kissinger method mainly characterizes the growth barrier in the crystallization [24]. Hence, Zr can restrain the nucleation of the second crystallization but promote its growth. In a word, the minor addition of Zr can improve the thermal stability of the present Fe-based alloys, which is possibly explained by the reinforced 'backbone' formed by Zr and boron [14].

The thermal expansion curves of the as-spun $(Fe_{0.78}Si_{0.09}B_{0.13})_{100-x}Zr_x$ ($x = 0$, 1 and 2) ribbons at a heating rate of 10 K/min are shown in Fig. 4. According to the shape of the thermal expansion curves, the dilatometric process can be divided

Table 3
Thermal parameters deduced from DSC scans with a heating rate of 10 K/min for Fe-based amorphous ribbons.

Alloys	T_x (K)	T_{p1} (K)	T_{p2} (K)	T_{p3} (K)	T_{p4} (K)	T_m (K)	T_l (K)	ΔT_m (K)	T_{rx}
$Fe_{78}Si_9B_{13}$(C0)	783	801	821	–	–	1412	1451	39	0.54
$(Fe_{0.78}Si_{0.9}B_{0.13})_{99}Zr_1$(C1)	815	827	881	938	973	1414	1434	20	0.57
$(Fe_{0.78}Si_{0.9}B_{0.13})_{98}Zr_2$(C2)	800	819	887	987	–	1418	1449	31	0.55

T_{rx}: T_x/T_l; ΔT_m: $T_l - T_m$.

Table 4
Apparent activation energies of Fe-based amorphous ribbons calculated by Kissinger method.

Alloys	E_{p1} (kJ/mol)	E_{p2} (kJ/mol)	E_{p3} (kJ/mol)	E_{p4} (kJ/mol)
$Fe_{78}Si_9B_{13}$(C0)	436	511	–	–
$(Fe_{0.78}Si_{0.9}B_{0.13})_{99}Zr_1$(C1)	560	344	439	577
$(Fe_{0.78}Si_{0.9}B_{0.13})_{98}Zr_2$(C2)	475	273	437	–

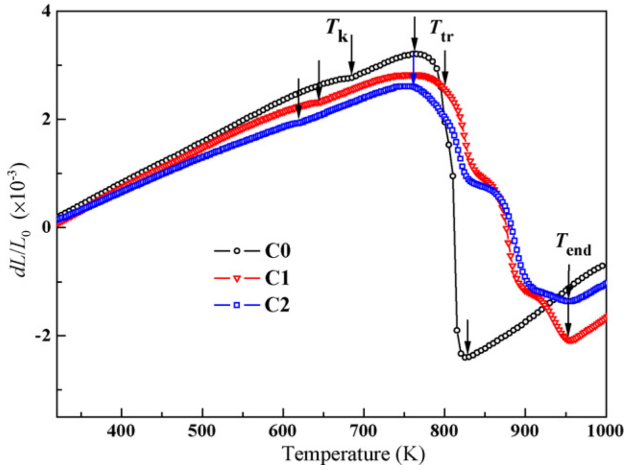

Fig. 4. Thermal expansion curves of the $(Fe_{0.78}Si_{0.09}B_{0.13})_{100-x}Zr_x$ ($x = 0$, 1 and 2) glassy alloys with a heating rate of 10 K/min.

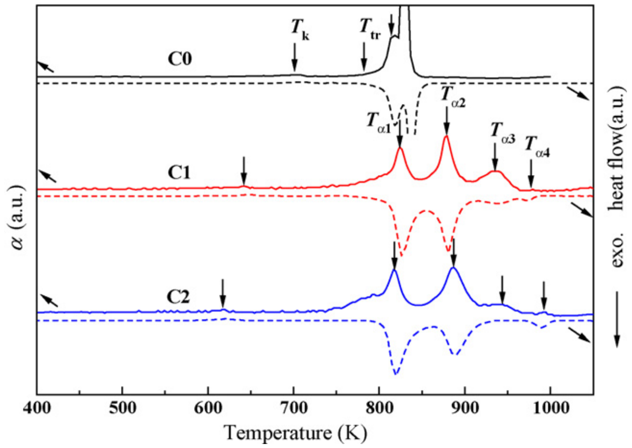

Fig. 5. Thermal expansion coefficients and DSC curves of $(Fe_{0.78}Si_{0.09}B_{0.13})_{100-x}Zr_x$ ($x = 0$, 1 and 2) glassy alloys with a heating rate of 10 K/min.

into four stages. The first stage is the linear expansion stage of the glassy alloys from room temperature to the inflection point T_k (denoted in Figs. 4 and 5). Here, the T_k of C0, C1 and C2 ribbons are 681, 643 and 613 K, respectively, showing a decreasing tendency with increasing c_{Zr}. The second stage is also a linear expansion stage from T_k up to the temperature of the first contraction, denoted by T_{tr}. The third stage starts from T_{tr} until the end temperature of the contraction, denoted by T_{end} in Fig. 4. In the third stage, the C0 alloy has two steps and its DIL curve drops more drastically than those of the C1 and C2 alloys. For the C1 and C2 alloys, the DIL curves of the contraction process have three stages over a wider temperature range than that of the C0 alloy, which are corresponding to the crystallization process in the DSC curves (Fig. 2).

In order to further investigate the contraction process of the present alloys, the thermal expansion coefficients (α) as a function of temperature at a heating rate of 10 K/min and the corresponding DSC curves at the same heating rate are shown in Fig. 5. Here, the peaks in α–T curves are denoted by $T_{\alpha1}$, $T_{\alpha2}$, etc. Obviously, the peak temperatures, especially $T_{\alpha1}$ and $T_{\alpha2}$, in the α–T curves are approximately consistent with the peak temperatures in the DSC curves, suggesting that the contraction process is mainly dependent on the crystallization process. He et al. find the similar contraction process in Zr–Ti–Cu–Ni–Be alloys [25].

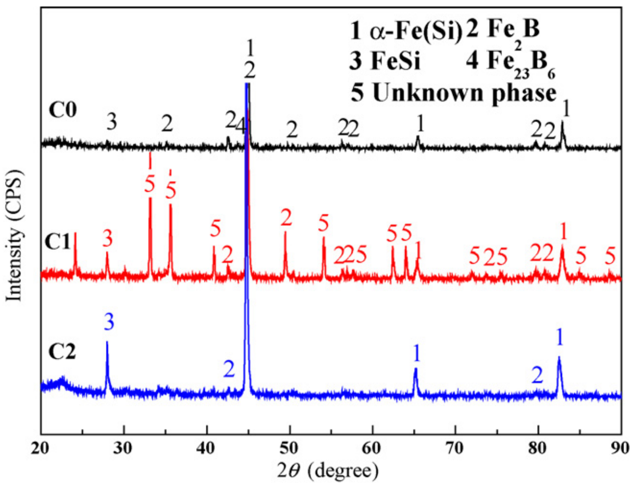

Fig. 6. XRD patterns of the fully crystallized $(Fe_{0.78}Si_{0.09}B_{0.13})_{100-x}Zr_x$ ($x = 0$, 1 and 2) glassy alloys after DIL measurement.

The fourth stage of the expansion curves starts from the end temperature (T_{end}) of the contraction process up to the limit of present measurement. In this stage, the samples are fully crystallized and the thermal expansion curves become a line again. The thermal expansion coefficient of the linear expansion region below Curie point (α_{amor}) and after fully crystallized (α_{cryst}) deduced from Fig. 4 by linearly fitting the DIL curves are listed in Table 5. The difference ($\Delta\alpha$) between α_{amor} and α_{cryst} are also listed in Table 5. Obviously, $\Delta\alpha$ varies in the order of C0 < C2 < C1, agreeing well with the Δd values.

Fig. 6 shows the XRD patterns of the fully crystallized $(Fe_{0.78}Si_{0.09}B_{0.13})_{100-x}Zr_x$ ($x = 0$, 1 and 2) ribbons after DIL measurement. By retrieving the ICDD PDF cards, the precipitated phases are α-Fe, Fe_2B, FeSi, $Fe_{23}B_6$ and unknown phases. Apparently, the types of precipitates of the C1 alloy are more than the C0 and C2 alloys.

Fig. 7 gives the M–H loops of the as-spun $(Fe_{0.78}Si_{0.09}B_{0.13})_{100-x}Zr_x$ ($x = 0$, 1 and 2) ribbons measured at room temperature. Apparently, three ribbons show a good soft magnetic property, i.e. a low coercivity (H_c) and a higher saturation magnetization (M_s). Compared with C0 and C1 ribbons, C2 ribbon seems more difficult to reach the saturation magnetization owing to the addition of the large Zr atoms. Fig. 8 gives the magnetization of C0, C1 and C2 ribbons as a function of temperature up to 750 K. With increasing temperature, a ferro-paramagnetic transition occurs above 600 K. Compared with C0 and C1 ribbons, the magnetization of C2 ribbon decreases more quickly. The inset shows the curves of $M^{1/0.36}$–T. According to Eq. (3), the Curie temperature T_c can be obtained by extrapolating the $M^{1/0.36}$–T line to the $M^{1/0.36} = 0$ line. Obviously, with increasing c_{Zr}, the M_s of the three samples varies in this order: C0 > C2 > C1, which is opposite to that

Table 5
Thermal expansion coefficient (α) below Curie point (α_{amor}) and after full crystallization (α_{cryst}), and the difference ($\Delta\alpha$) between α_{amor} and α_{cryst} of Fe-based amorphous ribbons with a heating rate of 10 K/min.

Alloys	α_{amor} ($\times 10^{-6}$ K^{-1})	α_{cryst} ($\times 10^{-6}$ K^{-1})	$\Delta\alpha$ ($\times 10^{-6}$ K^{-1})
$Fe_{78}Si_9B_{13}$(C0)	7.71	9.14	1.43
$(Fe_{0.78}Si_{0.9}B_{0.13})_{99}Zr_1$(C1)	7.67	10.26	2.59
$(Fe_{0.78}Si_{0.9}B_{0.13})_{98}Zr_2$(C2)	6.40	8.27	1.87

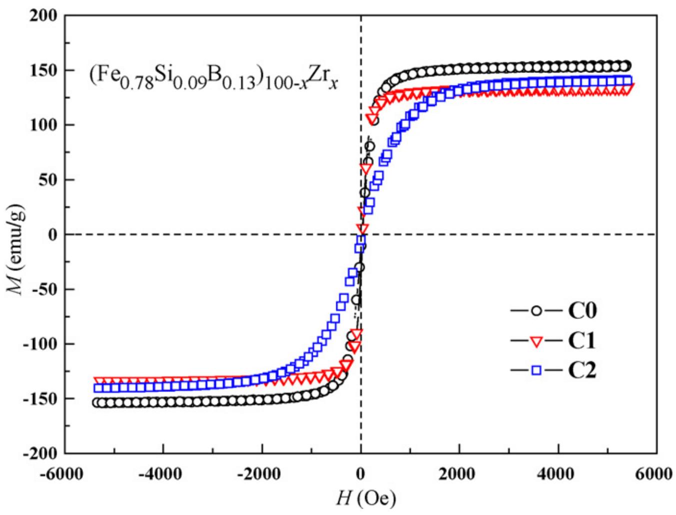

Fig. 7. M–H hysteresis loops of the as-spun $(Fe_{0.78}Si_{0.09}B_{0.13})_{100-x}Zr_x$ glassy alloys at room temperature.

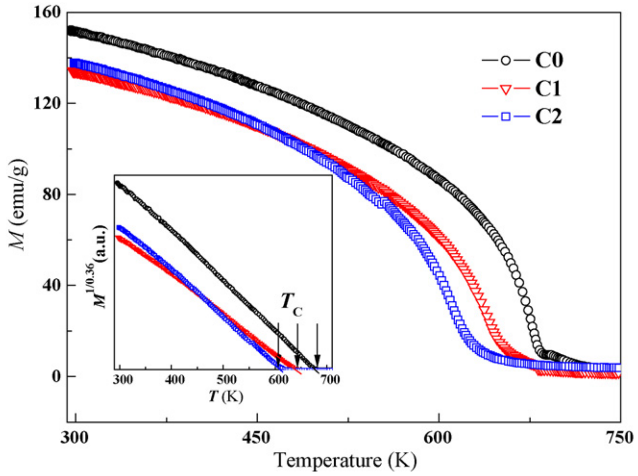

Fig. 8. Magnetization–temperature (M–T) curves of the $(Fe_{0.78}Si_{0.09}B_{0.13})_{100-x}Zr_x$ glassy alloys. The inset shows the curves of $M^{1/0.36}$–T.

Table 6

The saturation magnetization (M_s) deduced from M–H curves, the Curie temperature (T_c) deduced from DSC, DIL and M–T curves for as-spun Fe-based amorphous ribbons.

Alloys	M_s (emu/g)	T_c (K)		
		M–T	DSC	DIL
$Fe_{78}Si_9B_{13}$(C0)	154	678	685	681
$(Fe_{0.78}Si_{0.9}B_{0.13})_{99}Zr_1$(C1)	135	642	647	643
$(Fe_{0.78}Si_{0.9}B_{0.13})_{98}Zr_2$(C2)	141	612	620	613

of $\Delta\alpha$ and Δd. The M_s of three samples deduced from M-T loops are listed in Table 6. The T_c deduced from $M^{1/0.36}$–T curves as well as the $T_{c,dsc}$ and T_k deduced from DSC and DIL curves, respectively, are also listed in Table 6.

4. Discussions

4.1. Contraction behavior of as-spun Fe-based alloys

Under isochronal heating, the variation of sample length of the amorphous alloys is dependent on several factors: annihilation of the free volume, thermal expansion, structural relaxation, glass transition, viscous flow, and crystallization [25]. In Al-based amorphous alloys, the starting temperature T_{tr} of the contraction in the dilatation curve is corresponding to the glass transition temperature T_g in the DSC curve [26], which is explained by the argument that the Newtonian flow occurs in the supercooled region under the applied load [27]. In present work, the T_{tr} of C0, C1 and C2 ribbons deduced from Fig. 4 are 790, 806 and 793 K, respectively, which are slightly higher than the T_x of counterparts (Table 3), indicating that the contraction in the supercooled region of present Fe-based alloys, caused by the viscous flow under the applied load (25 cN), is much lower compared with Al-based glassy alloys.

As we know, the Young's modulus (K) shows the ability of the alloy to resist the deformation. For metallic glass, K can be calculated by [28]: $K^{-1} = \sum c_i K_i^{-1}$, here, K_i denotes the Young's modulus of the constituent elements obtained from Ref. [18]. The calculated K_{cal} of Al-based amorphous alloys in Ref. [26] is about 71 GPa, and the K_{cal} of the present alloys is about 114 GPa, which is much higher than that of the former. Hence, under applied load in the DIL measurement, the viscous flow in the supercooled region of the present alloys can be negligible. In other words, the contraction process in present work is mainly ascribed to the crystallization process, which is indicated by DIL and DSC curves (Figs. 4 and 5).

4.2. Deviation degree from the equilibrium state of as-spun Fe-based ribbons

As above mentioned, the d_{cal} of the ribbons is averaged from the covalent radii of the constituent elements in the crystalline state. Therefore, the Δd of the samples can be assumed as a parameter to scale the deviation degree (D_{dev}) away from the crystalline state, i.e. equilibrium state, of the measured alloys. As shown in Table 1, the Δd of the ribbons changes in the order of C0 < C2 < C1, implying that the D_{dev} of the ribbons varies in the same order: C0 < C2 < C1. In addition, the larger the D_{dev}, the higher number of the possible ways to experience in the crystallization. Hence, it can be explained that the number of the types of crystallized phases of C1 ribbon is highest among three ribbons (Fig. 6). Based on the expansion curves (Fig. 4), the difference of the expansion coefficient $\Delta\alpha$ of the ribbons between the amorphous and fully crystallized state varies in the order: C0 < C2 < C1 (Table 5), which is consistent with Δd and confirming the maximum deviation degree of C1 ribbon from the equilibrium state.

According to the two-structure model [29], iron atoms exist in the amorphous state with face-centered-cubic (fcc) and body-centered-cubic (bcc) structural units simultaneously. From Fig. 6, the major phase of the fully crystallized ribbons is bcc-Fe. Hence, the larger deviation degree from the equilibrium state, the lower amount of bcc-Fe structural unit and the less bcc-Fe nuclei in the ribbons. It is expected that C1 ribbon exhibits the highest T_x and T_{rx} (Table 3), suggesting that the best glass thermal stability among three ribbons. From the viewpoint of atomic ordering during the devitrification of the Fe-based glasses [30], the larger D_{dev}, the larger energy barrier to overcome. Hence, it can be understood that the apparent energy E_{p1} for the first crystallization changes in the order of C0 < C2 < C1 (Table 4), consistent with that of the D_{dev} of the ribbons.

It is known that bcc-Fe is ferromagnetic, but fcc-Fe is paramagnetic with a much lower M_s than bcc-Fe at room temperature [31]. Meanwhile, considerable molecular dynamic simulations showed that the fcc and bcc structures are dominant components in the Fe-based alloys [32]. Accordingly, it is reasonable to assume that the fcc and bcc structural units in the amorphous state have a similar properties as the fcc and bcc iron. As indicated by Δd, $\Delta\alpha$, T_x, T_{rx} and E_{p1}, C1 ribbon is furthest from the equilibrium state and has the lest bcc structural units, hence, it is expected that C1 exhibits a lowest M_s and the M_s of the ribbons changes in an order exactly opposite to that of the D_{dev} parameters (Tables 1, 5 and 6).

4.3. Curie temperature of the Fe-based ribbons indicated by M-T, DSC and DIL curves

It is shown that the inflection temperatures (T_k) in DIL curves are according well with T_c indicated by the *M–T* curves (Table 6). Combining the $T_{c,dsc}$ in Fig. 2a, the T_c of the present alloys can also be scaled by $T_{c,dsc}$ and T_k in DSC and DIL curves respectively. Comparing Fig. 2a, 4 and 8, it is found that the resolution of Curie temperature increase in this order: DSC < DIL < *M–T* measurement.

From Table 2, it can be seen that the $T_{c,dsc}$ of the C0 alloy decreases with increasing the heating rate. Greer [33] has found the same result in the $Fe_{81.5}B_{16.5}Si_4$ glassy alloys. However, the $T_{c,dsc}$ of the C1 and C2 alloys at different heating rates is almost a constant with deviations within 2 K. According to Greer's argument, T_c is associated with the degree of the structural relaxation: the higher the heating rate, the less the sufficient structure relaxation, the lower the T_c. Hence, due to the large atomic radius and the high negative mixing enthalpy with other elements in present alloys [14,34], Zr will suppress the atomic rearrangement, weaken the relaxation degree, and thereby result in little change of the Curie temperature of C1 and C2 ribbons with increasing the heating rate (Table 2).

In the ferro-paramagnetic transition process, the negative spontaneous magnetostriction with increasing temperature, namely known the Invar anomalous expansion behavior, results in the decrement of the mean atomic spacing above the Curie point [35,36]. Consequently, due to the mean atomic spacing below the Curie point is larger than that above the Curie point, the thermal expansion curves exhibit an inflection at T_k (Fig. 4). In other words, the Curie temperature of the Fe-based glassy alloys can be scaled by T_k in DIL measurement.

As shown in Fig. 8 and Table 6, the T_c of the ribbons decreases with increasing c_{Zr}, showing a different changing behavior from their M_s. In addition, compared with C0 and C1 ribbons, C2 ribbon has a larger difficulty to reach the saturation magnetization in *M–H* loops (Fig. 7), and has a quick drop of magnetization to zero in the *M–T* curve (Fig. 8). These abnormal behaviors of C2 ribbon should be associated with the existing details of the large Zr atoms in the amorphous phase, but they are difficult to be explained by present observations and worthy of the further study in future.

5. Conclusions

The thermal stability, thermal behavior and magnetic properties of the $(Fe_{0.78}Si_{0.09}B_{0.13})_{100-x}Zr_x$ (x = 0, 1 and 2) glassy alloys were studied by the experimental techniques such as XRD, DSC, DIL and VSM, and the new conclusion have been obtained as follows:

1. The DSC results show that 1 at.% Zr addition can improve the thermal stability of the present Fe-based glassy alloys, but the further addition of Zr deteriorates the thermal stability. The DIL curves of the present Fe-based glassy alloys show that the contraction behavior in heating process is dominated by the crystallization process.
2. With increasing c_{Zr}, the Δd, $\Delta\alpha$, T_x, T_{rx}, and E_{p1} of the present alloys first increase and then decrease, which is opposite to the change of M_s. The non-monotonic variation of these parameters can be explained by the deviation degree from the equilibrium state of the present Fe-based glassy alloys.
3. The $T_{c,dsc}$ in DSC curves and T_k in dilatation curves of the present alloys accord well with T_c indicated by the *M–T* curves, showing that the T_c of present alloys decreases with increasing c_{Zr}.

Acknowledgments

The authors acknowledge the National Natural Science Foundation (Nos. 50871061, 50871062, 50831003, 50631010 and 50801041), the Shandong Excellent Youth Award Foundation (No. 2008BS04020), the project NCET-06-584 and the National Basic Research Program of China (973 Program) (2007CB613901) for financial supports.

References

[1] V. Ponnambalam, S.J. Poon, G.J. Shiflet, V.M. Keppens, R. Taylor, G. Petculescu, Appl. Phys. Lett. 83 (2003) 1131–1133.
[2] Z.P. Lu, C.T. Liu, J.R. Thompson, W.D. Porter, Phys. Rev. Lett. 92 (2004) 245503.
[3] A. Makinoa, C.T. Chang, T. Kubota, A. Inoue, J. Alloys Compd. 483 (2009) 616–619.
[4] W. Zhang, A. Inoue, Appl. Phys. Lett. 80 (2002) 1610.
[5] N.O. Gonchukova, A.N. Drugov, Glass Phys. Chem. 29 (2003) 184.
[6] D. Schermeyer, H. Neuhauser, Mater. Sci. Eng. A 226–228 (1997) 846.
[7] K. Ota, W.J. Botta, G. Vaughan, A.R. Yavari, J. Alloys Compd. 388 (2005) 11–13.
[8] G. Wilde, S.G. Klose, W. Soeline, G.P. Gorler, K. Jeropoulos, R. Willinecker, H.J. Fecht, Mater. Sci. Eng. A 226 (1997) 434–438.
[9] C. Nagel, K. Ratzke, E. Schmidtke, F. Faupel, Phys. Rev. B 60 (1999) 009212.
[10] A.K. Varshneya, Fundamentals of Inorganic Glasses, Academic Press, San Diego, CA, 1994.
[11] H.J. Ma, W.M. Wang, J.T. Zhang, G.H. Li, L.N. Hu, Y.C. Niu, J. Alloys Compd. 485 (2009) 255–260.
[12] T. Itoi, A. Inoue, Mater. Trans. JIM 41 (2000) 1256.
[13] B.L. Shen, C.T. Chang, Z.F. Zhang, A. Inoue, J. Appl. Phys. 102 (2007) 023515.
[14] S.J. Poon, G.J. Shiflet, F.Q. Guo, V. Ponnambalam, J. Non-Cryst. Solids 317 (2003) 1–9.
[15] C. Birac, Phys. Stat. Sol. A 36 (1975) 247.
[16] Y.C. Niu, X.F. Bian, W.M. Wang, S.F. Jin, X.J. Liu, J.Y. Zhang, G.L. Qin, J. Non-Cryst. Solids 351 (2005) 3854–3860.
[17] G. Herzer, IEEE Trans. Mag. 25 (1989) 3327–3329.
[18] http://www.webelements.com.
[19] Y.C. Niu, X.Y. Bian, W.M. Wang, S.F. Jin, G.H. Li, F.M. Chu, W.G. Zhang, J. Alloys Compd. 433 (2007) 296–301.
[20] T.D. Shen, R.B. Schwarz, Acta Mater. 49 (2001) 837–847.
[21] L.C. Zhang, J. Xu, J. Non-Cryst. Solids 347 (2004) 166–172.
[22] J. Steinberg, S. Tyagia, A.E. Lord, Acta Metall. 29 (1981) 1309.
[23] H.R. Wang, Y.L. Gao, G.H. Min, X.D. Hui, Y.F. Ye, Phys. Lett. A 314 (2003) 81–87.
[24] A.A. Sdiman, S. Al-Heniti, A. Al-Hajry, M. Al-Assiri, G. Al-Barakati, Thermochim. Acta 413 (2004) 57.
[25] Y. He, R.B. Schwarz, D.G. Mandrus, J. Mater. Res. 11 (1996) 1836.
[26] G.H. Li, W.M. Wang, X.F. Bian, J.T. Zhang, R. Li, L. Wang, J. Alloys Compd. 478 (2009) 745–749.
[27] Y. Kawamura, T. Nakamura, H. Kato, H. Mano, A. Inoue, Mater. Sci. Eng. A 304–306 (2001) 674–678.
[28] Y.X. Wei, B. Zhang, R.J. Wang, M.X. Pan, D.Q. Zhao, W.H. Wang, Scripta Mater. 54 (2006) 600.
[29] W.M. Wang, W.X. Zhang, A. Gebert, S. Roth, C. Mickel, L. Schultz, Metall. Mater. Trans. A 40 (2009) 511.
[30] R.C. O'Handley, J. Appl. Phys. 62 (1987) R15–R49.
[31] J.J. Xu, Analysis of the Metallic Physical Properties, Shanghai Science and Technology Press, Shanghai, 1988, p. 98.
[32] H. Li, Phys. Rev. B 68 (2003) 024210.
[33] A.L. Greer, J. Mater. Sci. 17 (1982) 1117–1124.
[34] A. Takeuchi, A. Inoue, Mater. Trans. JIM 41 (2000) 1372–1378.
[35] F.E. Luborsky, in: C. Ke, Y.C. Tang, Y. Luo, K.Y. He (Eds.), Amorphous Metallic Alloy, Metallurgical Industry Press, Beijing, 1989, p. 232.
[36] W.D. Zhong, Ferromagnetism (II), Science Press, Beijing, 2000, pp. 26–27.